

Article

Heterostructured Bi₂O₃@rGO Anode for Electrochemical Sodium Storage

Benrong Hai and Changsheng Liu * 

School of Materials Science and Engineering, Northeastern University, Shenyang 110819, China; hbr1019@163.com

* Correspondence: cslu@mail.neu.edu.cn

Abstract: Bismuth oxide (Bi₂O₃) is an auspicious anode material for sodium-ion batteries owing to its high theoretical capacity and abundant Bi resources. However, the poor electronic conductivity and huge volume expansion of Bi₂O₃ during cycling lead to the low coulombic efficiency and unstable cycling stability. Aiming to suppress these issues, we use highly conductive reduced graphene oxide (rGO) as a continuous skeleton to fabricate a Bi₂O₃@rGO heterostructure. It exhibits high reversibility and stability for electrochemical sodium storage by delivering a reversible capacity of 161 mAh g⁻¹ after 100 cycles at 50 mA g⁻¹, which completely outperforms Bi₂O₃ (43 mAh g⁻¹). In addition, the coulombic efficiency of the heterostructure stabilizes at >90% upon only 3 cycles. The results can be attributed to the dual function of rGO in supporting Bi₂O₃ nanoparticles and providing conductive pathways to fasten electron transport.

Keywords: sodium-ion battery; bismuth oxide; alloy; reduced graphene oxide; coulombic efficiency

1. Introduction

Energy storage technologies are of high importance to meet currently flourishing energy demand and environmental pollution consequences depletion of fossil fuels. Lithium-ion batteries (LIBs), owing to high-energy densities and excellent long-term cycle life, have been main energy storage medium in the past decade [1]. LIBs show great performance and dominate the market of portable electronics, but the limited resources and uneven global distributions of lithium have raised serious concern on the sustainability of the LIB technology [2]. Thus, it is highly urgent to research new energy storage systems based on more abundant elements. Sodium-ion batteries (SIBs) have focused global attention since Na is widely distributed and SIBs exhibit competitive performance to LIBs. In particular, SIBs are cost-competitive to meet future large-scale energy storage requirements [3]. However, in comparison with lithium ion, sodium ion has a larger ionic radius (1.02 Å), it's more arduous challenges to develop appropriate materials for reversible and fast sodium ion insertion/extraction. And for the anode materials, huge volume expansion and sluggish kinetics during cycling process may result in fast capacity attenuation and low coulombic efficiency [4].

In recent decades, a large amount of effort has been made to develop brilliant anode materials. Carbonaceous materials [5,6], metal sulfides [7,8], metal oxides [9,10] and metal phosphides [11,12] have been extensively researched as anodes for SIBs. Among them, alloy-based metal oxides are attractive as anode materials for SIBs, due to low redox potential, high volumetric energy density and theoretical specific capacity [13]. Bi₂O₃ has been reported as an auspicious anodes owing to its high gravimetric specific capacity, abundant resources and environmental sustainability [14]. Deng et al. synthesized bismuth oxide/reduced graphene oxide nanocomposites as an electrode for LIBs, which deliver a capacity of 347.3 mAh g⁻¹ with 79% capacity retention (after 100 cycles at 600 mA g⁻¹) [15]. Kim et al. prepared Bi₂O₃/carbon composites as an anode for SIBs by simple ball-milling method. The Bi₂O₃/carbon electrode exhibited a high capacity of 440 mAh g⁻¹ after



Citation: Hai, B.; Liu, C.

Heterostructured Bi₂O₃@rGO Anode for Electrochemical Sodium Storage.*Materials* **2022**, *15*, 2787. <https://doi.org/10.3390/ma15082787>

Academic Editor: Enrico Negro

Received: 26 February 2022

Accepted: 6 April 2022

Published: 11 April 2022

Publisher's Note: MDPI stays neutral with regard to jurisdictional claims in published maps and institutional affiliations.



Copyright: © 2022 by the authors. Licensee MDPI, Basel, Switzerland. This article is an open access article distributed under the terms and conditions of the Creative Commons Attribution (CC BY) license (<https://creativecommons.org/licenses/by/4.0/>).

20 cycles at 714.3 mA g^{-1} [16]. However, metal oxides still suffer from inherent problems of unsatisfactory electronic conductivity, sluggish Na-ion transfer rate and severe volume expansion during cycling processes [17]. To address these issues, many optimized architectures have been constructed by researchers, such as hybridizing with carbonaceous matrix [18,19], compositing with different materials [20] and designing appreciated structures [21,22]. Among these, the heterostructure constructed by active material and carbonaceous substrate is one of the most promising structures for SIBs [23]. RGO stands out among various carbonaceous matrices because of its fast electron mobility, ideal large specific surface area and high charge carrier mobility. It was reported that alloy-based metal oxide@rGO composite electrodes have significantly improved the electrochemical performance of SIBs [24]. For example, 3D SnO_2 @rGO composites with a large amount of internal void space are prepared to resolve the huge volume deformation problem of SnO_2 -based materials as anodes for SIBs [25]; the Fe_2O_3 /holey rGO anode for SIBs exhibits excellent cyclability and rate capability owing to the introduction of wrinkled rGO, since wrinkles of graphene layers act as a template for anchoring Fe_2O_3 nanoparticles and effectively relax the strain induced by the volume deformation [26].

In this work, we report that the Bi_2O_3 @rGO heterostructure exhibits drastically enhanced sodium storage in comparison with bare Bi_2O_3 particles. As shown in Figure 1, Bi_2O_3 nanoparticles are anchored on the rGO layer with a large surface area. This enables the shortening of the Na-ion diffusion length and increases the contact with electrolyte. Meanwhile, rGO layers with high electrical conductivity can improve electron diffusion and serve as a skeleton to prevent the shedding or agglomeration of Bi_2O_3 nanoparticles during cycling. As a result, the Bi_2O_3 @rGO heterostructure electrode exhibits an excellent coulombic efficiency (EC) reaching $> 90\%$ after 3 cycles and a good cycling ability of 160.9 mAh g^{-1} after 100 cycles at 50 mA g^{-1} .

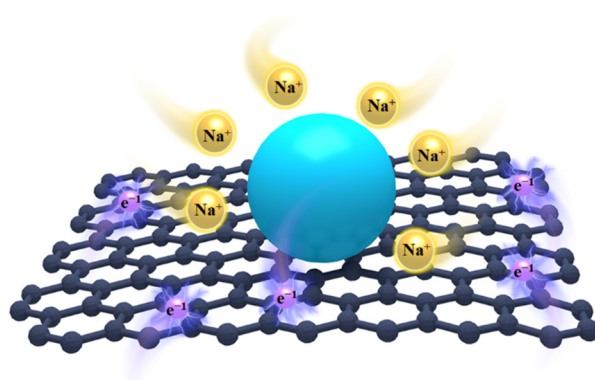


Figure 1. Schematic of Na-ion and electron transfer in Bi_2O_3 @rGO.

2. Materials and Methods

2.1. Synthesis of Bi_2O_3 @rGO

Modified Hummers method was adopted to prepare graphene oxides (GO) [27,28]. The Bi @rGO precursor was synthesized by a typical hydrothermal method. GO (50 mg) was ultrasonically dispersed in N,N -dimethylformamide (40 mL), followed by adding $\text{Bi}(\text{NO}_3)_3 \cdot 5\text{H}_2\text{O}$ (100 mg) and polyvinylpyrrolidone (300 mg) into the dispersion, then stirred until completely dissolved. The turbid liquid was moved to a Teflon-lined stainless-steel autoclave and heated ($180 \text{ }^\circ\text{C}$, 8 h). After cooling down, the obtained precipitate was washed and dried. The Bi_2O_3 @rGO heterostructure was obtained by a further annealing treatment of the resulting precursor at $300 \text{ }^\circ\text{C}$ for 4 h ($5 \text{ }^\circ\text{C min}^{-1}$) in ambient air. Bi_2O_3 particles were prepared under the same conditions without GO.

2.2. Structural Refinement

X-ray diffraction (XRD) was performed on a Bruker-axs Discover D8 (Rigaku, Japan) with $\text{Cu K}\alpha$ (1.54056 \AA). Renishaw Raman Spectrometer (HORIBA, Kyoto, Japan) employ-

ing visible excitation at 532 nm was used to record the Raman spectrum. X-ray photoelectron spectroscopy (XPS) was measured with a Thermo Fisher Nexsa X-ray photoelectron spectrometer (Thermo Fisher, Waltham, MA, USA), which is equipped with a monochromatic Al K α X-ray (1486.6 eV). Scanning electron microscopy (SEM) images were obtained by utilizing a Hitachi S4800 (Hitachi, Japan). Transmission electron microscopy (TEM) was achieved on a JEOL 2100F (JEOL, Kyoto, Japan) transmission electron microscope.

2.3. Electrochemical Investigation

Electrodes were prepared by dispersing Bi₂O₃@rGO (80 wt%), Super-P (10 wt%) and polyvinylidene fluoride dissolved in N-methylpyrrolidinone (10 wt%). The obtained slurry was coated on a copper foil, pressed and vacuum-dried at 110 °C, and the mass loading was around 1 mg cm⁻². Electrochemical tests were performed using CR2032 coins, which were assembled in a nitrogen-filled glovebox (oxygen and moisture concentrations < 0.1 ppm). A glass microfiber filter (pore size ~1 μ m) was employed to separate the sodium metal disk counter electrode from the electrode. A total of 1 M sodium perchlorate in ethylene carbonate/propylene carbonate (1:1) was prepared as electrolyte. Electrochemical impedance spectroscopy (EIS) and cyclic voltammetry (CV) were measured on a Bio-Logic VSP electrochemical workstation, and the CVs were between 0.01–2.5 V (vs. Na⁺/Na). Galvanostatic charge-discharge was measured on a Land battery testing system (CT2001A, Land, China) in a potential range of 0.01–2.5 V (vs. Na⁺/Na). The EIS was carried out with an amplitude of 5 mV at open-circuit voltage and the frequency range was 10 mHz–100 kHz.

3. Results

3.1. Morphology, Structure and Composition Analysis

Crystalline structure and phase purity of Bi₂O₃@rGO heterostructure are characterized by XRD. The XRD pattern of Bi₂O₃@rGO (Figure 2a) matches well with the peaks of tetragonal δ -Bi₂O₃ (JCPDS 27-0050) at $2\theta = 27.9^\circ$ (201), 31.8° (002), 32.7° (220), 46.2° (222), 46.9° (400), 54.3° (203), 55.5° (421), and 57.8° (402). It has been reported that δ -Bi₂O₃ exhibits the fastest oxygen ion conduction in the six polymorphs of Bi₂O₃ [29]. No peaks of Bi (Figure A1) are observed, suggesting high purity of the material, and that Bi has been completely converted to Bi₂O₃ after annealing treatment [30,31]. Figure 2b displays the Raman spectra of Bi₂O₃@rGO and GO. The D band (1350 cm⁻¹) and G band (1590 cm⁻¹) confirm the presence of rGO in the composite. The surface chemistry and interaction between Bi₂O₃ and the rGO layers are further investigated by XPS measurements. The existence of Bi, C and O elements are indicated in Figure 2c. The high-resolution XPS spectrum (Figure 2d) for Bi 4f exhibits two peaks located at 158.9 and 164.2 eV, attributed to the Bi 4f_{7/2} and Bi 4f_{5/2}, respectively. In Figure 2e, the C 1s spectrum of Bi@rGO shows four peaks of sp² C (284.8 eV), C-C (285.9 eV), C=O (287.8 eV) and O-C=O (289.3 eV) [14]. The C 1s spectrum is consistent with the FTIR result in Figure A2. The peaks for O1s could be fitted into three sub peaks at about 530.4, 531.8 and 533.6 eV (Figure 2f), which correspond to the Bi-O band, carbonyl and hydroxyl/epoxy, respectively [18].

Figures 3a and A3a represent the SEM images of Bi₂O₃@rGO where Bi₂O₃ nanoparticles are well anchored on rGO layers without agglomeration, presumably due to electrostatic repulsion that keeps sufficient space between Bi₂O₃ nanoparticles. The SEM images of Bi₂O₃@rGO show similar morphology features to that of Bi@rGO (Figure A3b), indicating that the anneal process at 300 °C in ambient air does not damage the morphologies of either Bi₂O₃ nanoparticles or rGO layers. In contrast, bare Bi₂O₃ particles (Figure A3c) agglomerate without rGO, forming clusters with a size of multiple micrometers after annealing from Bi particles (Figure A3d). The structure of Bi₂O₃@rGO is further manifested by TEM image (Figure 3b). Bi₂O₃ nanoparticles are uniformly distributed on rGO, and the wrinkles of rGO can be clearly seen, indicating that the layers are thin. Once again, the agglomeration of Bi₂O₃ nanoparticles is effectively prevented with the presence of rGO and the size of Bi₂O₃ nanoparticles in the composite is less than 100 nm. The high-resolution TEM image in Figure 3c exhibits that the lattice spacing is 0.32 nm, corresponding to the

(201) plane of δ - Bi_2O_3 . The EDS mapping of the selected region (indicated by the red frame in Figure 3b) is shown in Figure 3e–g, which further demonstrates the successful fabrication of the Bi_2O_3 @rGO composite.

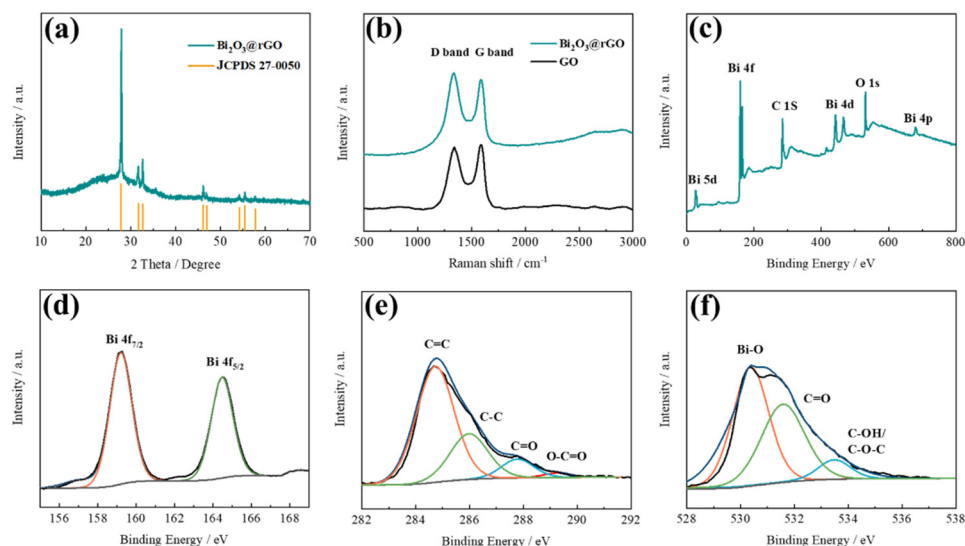


Figure 2. (a) XRD pattern of Bi_2O_3 @rGO. (b) Raman spectra of Bi_2O_3 @rGO and GO. (c) XPS survey of Bi_2O_3 @rGO. High resolution XPS spectra for (d) Bi, (e) C and (f) O elements of Bi_2O_3 @rGO.

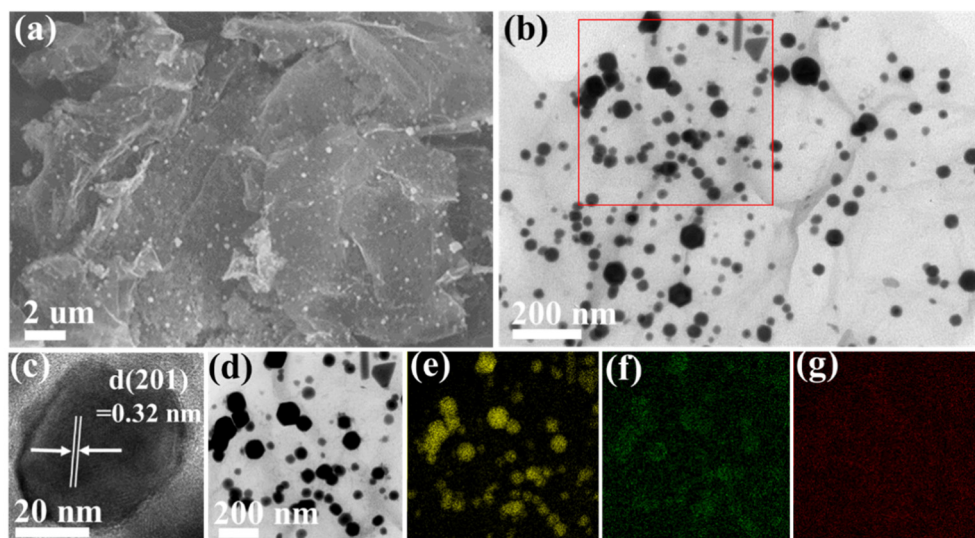


Figure 3. (a) SEM image of Bi_2O_3 @rGO. (b) TEM and (c) high-resolution TEM images of Bi_2O_3 @rGO. (d) The selected region in (b) and EDS mapping of (e) Bi, (f) O, (g) C.

3.2. Sodium Storage Behavior

The CV curves of the composite are shown in Figure 4a. The peak observed at 1.06 V in the first cathodic scan corresponds to the reduction of Bi_2O_3 to Bi and the formation of SEI film. The peak at 0.52 V is attributed to the alloy reaction process from Bi to NaBi and the peak located at 0.30 V corresponds to NaBi to produce Na_3Bi [32]. The peaks at 0.72 V and 0.82 V are caused by the desodiation of $\text{Na}_3\text{Bi} \rightarrow \text{NaBi} \rightarrow \text{Bi}$ [33]. The overlapping curves of the third and fifth cycles reveal the good reversibility of the composite. Figure 4b exhibits the initial three discharge-charge profiles of Bi_2O_3 @rGO at 50 mA g^{-1} and the initial discharge capacity is 421.8 mAh g^{-1} . Two discharge plateaus (0.52 and 0.30 V) and two charge plateaus (0.72 and 0.82 V) are in good agreement with the CV curves of Bi_2O_3 @rGO. The initial three charge-discharge profiles of Bi_2O_3 at 50 mA g^{-1} (Figure A4)

show an initial discharge capacity of 383.6 mAh g^{-1} . As seen, the discharge capacities at the second and third cycles are 186.8 and 162.5 mAh g^{-1} , respectively. This suggests that the Bi_2O_3 electrode without rGO has a mass of irreversible capacity in the first two discharge–charge cycles. In comparison with Bi_2O_3 , the $\text{Bi}_2\text{O}_3@\text{rGO}$ electrode shows better capacity retention in the early cycles. The fact that the introduction of rGO can effectively mitigate the rapid capacity decay is also reported by other studies [32,34].

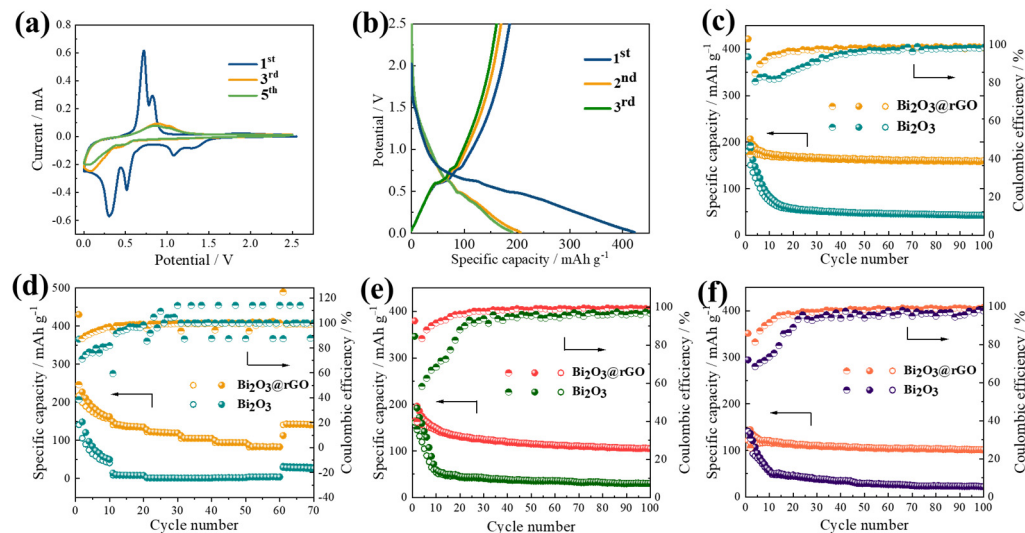


Figure 4. (a) CV curves and (b) discharge–charge profiles of $\text{Bi}_2\text{O}_3@\text{rGO}$. (c) Cycle performance of $\text{Bi}_2\text{O}_3@\text{rGO}$ and Bi_2O_3 at 50 mA g^{-1} . (d) Rate performance of $\text{Bi}_2\text{O}_3@\text{rGO}$ and Bi_2O_3 at 50 mA g^{-1} . Cycle performance at (e) 200 mA g^{-1} and (f) 1 A g^{-1} .

To investigate the performance of $\text{Bi}_2\text{O}_3@\text{rGO}$ composites and bare Bi_2O_3 particles for SIBs, the cycle performance and rate capability are evaluated. The $\text{Bi}_2\text{O}_3@\text{rGO}$ exhibits a reversible discharge capacity of 160.9 mAh g^{-1} after 100 cycles (Figure 4c), which is higher than those of the Bi_2O_3 ($<50 \text{ mAh g}^{-1}$) and rGO electrode (Figure A5, $\sim 100 \text{ mAh g}^{-1}$). It has also been reported that the introduction of a carbon-based material can more effectively enhance the reversible capacity of the composite than bare Bi_2O_3 [16,31]. However, there are few discussions about the CE of Bi_2O_3 -based materials. In this work, the initial CE of $\text{Bi}_2\text{O}_3@\text{rGO}$ is 42.51%, due to the formation of SEI and electrolyte decomposition. The CE rapidly increases to 90.0% after 3 cycles and stabilizes at $>95\%$ after 6 cycles, whereas the CE of Bi_2O_3 is 89.2% even after 13 cycles. Figure 4d describes the rate capability of $\text{Bi}_2\text{O}_3@\text{rGO}$ and Bi_2O_3 . The composite electrode delivers specific capacities of 162, 135, 119, 105, 94 and 83 mAh g^{-1} at 0.05, 0.1, 0.2, 0.5, 1, and 2 A g^{-1} , respectively. As seen, the capacity recovers to 141 mAh g^{-1} when the current density reduces to 0.05 A g^{-1} . In contrast, the capacity of bare Bi_2O_3 quickly drops to about 10 mAh g^{-1} at 0.2 A g^{-1} , due to the deteriorated electron transfer at high current densities and the unconstrained volume expansion of Bi_2O_3 without the presence of rGO. The capacities of pure rGO (Figure A6) are also much lower than those of the composite at all current densities. Furthermore, the composite shows good cycling stability at higher current densities, delivering stable capacities of 105 and 97.98 mAh g^{-1} at 0.2 and 1 A g^{-1} , respectively (Figure 4e,f), completely outperforming the Bi_2O_3 .

Figure 5a compares the discharge capacities of $\text{Bi}_2\text{O}_3@\text{rGO}$ and Bi_2O_3 electrodes after 100 cycles at different current densities. It is evident that the $\text{Bi}_2\text{O}_3@\text{rGO}$ electrode exhibits much better cycle performance than the Bi_2O_3 electrode. Furthermore, the CEs in the first 10 cycles (Figure 5b) clearly shows that the CE of the $\text{Bi}_2\text{O}_3@\text{rGO}$ electrode increases much more rapidly than that of the Bi_2O_3 at all tested current densities. Meanwhile, the CE also remains higher for the former than the latter and is responsible for the better cycling stability of the former. To further explicate the improved electrochemical performance of

$\text{Bi}_2\text{O}_3@\text{rGO}$, the Nyquist plots of the two samples are presented in Figure 5c. The Nyquist plots of $\text{Bi}_2\text{O}_3@\text{rGO}$ and Bi_2O_3 have similar shapes, consisting of a semicircle in the high-frequency region and a straight line in the low-frequency region. Obviously, $\text{Bi}_2\text{O}_3@\text{rGO}$ composites have a smaller charge-transfer resistance (R_{ct}) value than bare Bi_2O_3 , confirming that the incorporation of Bi_2O_3 nanoparticles into rGO layers is beneficial to improve the rapid electron transfer during cycling.

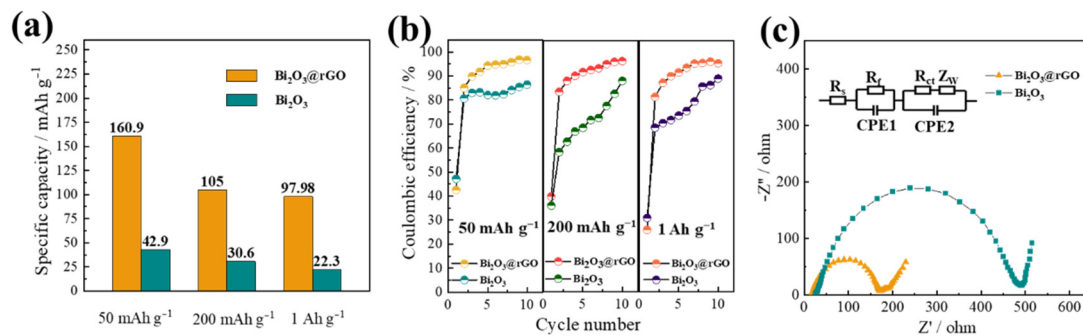


Figure 5. The comparison of (a) discharge capacities and (b) CEs of $\text{Bi}_2\text{O}_3@\text{rGO}$ and Bi_2O_3 . (c) Nyquist plots of $\text{Bi}_2\text{O}_3@\text{rGO}$ and Bi_2O_3 after 100 cycles at 50 mA g⁻¹.

To further confirm the cycle stability of the composite, we have taken SEM images of $\text{Bi}_2\text{O}_3@\text{rGO}$ before and after 100 cycles at 50 mA g⁻¹ (Figure 6a,b). Figure 6b shows that Bi_2O_3 nanoparticles are still uniformly anchored on rGO layers with strong contact and kept clear shape. Schematic illustration of the deformation of Bi_2O_3 and $\text{Bi}_2\text{O}_3@\text{rGO}$ after cycling is displayed in Figure 6c. In the absence of rGO layers, Bi_2O_3 particles deform after cycling, which could lead to unstable coulombic efficiency as well as inferior cycling stability. The presence of rGO layers can suppress volume expansion of Bi_2O_3 nanoparticles during cycling and reduce particle aggregation, contributing to better CE and cycle performance of $\text{Bi}_2\text{O}_3@\text{rGO}$.

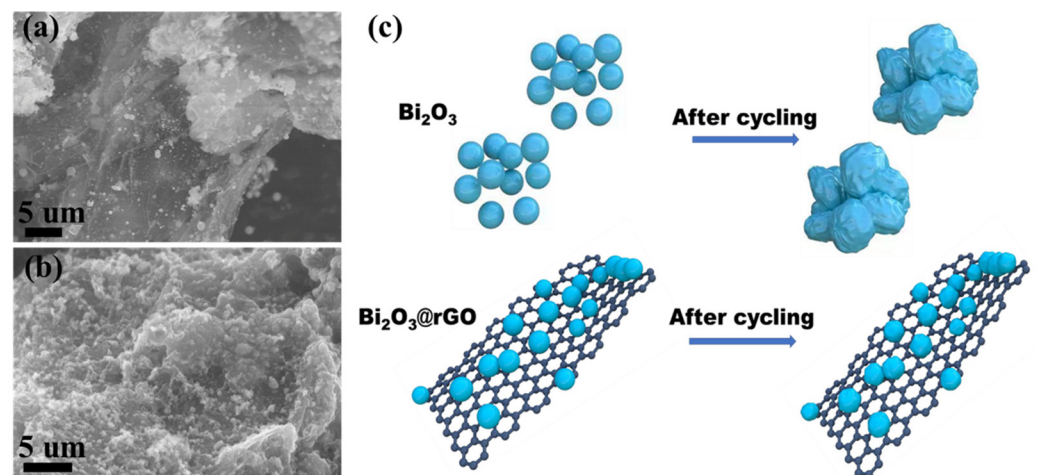


Figure 6. SEM images of $\text{Bi}_2\text{O}_3@\text{rGO}$ (a) before cycling and (b) after cycling. (c) Schematic of the deformation of the two samples after cycling.

4. Conclusions

In summary, a $\text{Bi}_2\text{O}_3@\text{rGO}$ heterostructure was prepared and applied as a composite anode for SIBs. The anode exhibited a reversible capacity of 160.9 mAh g⁻¹ after 100 cycles at 50 mA g⁻¹ and its CE rapidly increased to >90% after 3 cycles. Both the cycle performance and CE are much enhanced compared with bare Bi_2O_3 particles used as an anode. The enhancement is attributed to rGO layers which act as a conductive template, shorten the diffusion length of Na-ion, and effectively suppress the agglomeration of Bi_2O_3

nanoparticles during the charge-discharge process. Our method demonstrates a synergy between the active material and the 2D conductive template and has the potential to be applied for a wide range of SIB electrode materials.

Author Contributions: Conceptualization, B.H.; writing—original draft preparation, B.H.; writing—review and editing, B.H.; supervision, C.L.; funding acquisition, C.L. All authors have read and agreed to the published version of the manuscript.

Funding: This research received no external funding.

Institutional Review Board Statement: Not applicable.

Informed Consent Statement: Not applicable.

Data Availability Statement: The data presented in this study are contained within the article.

Conflicts of Interest: The authors declare no conflict of interest.

Appendix A

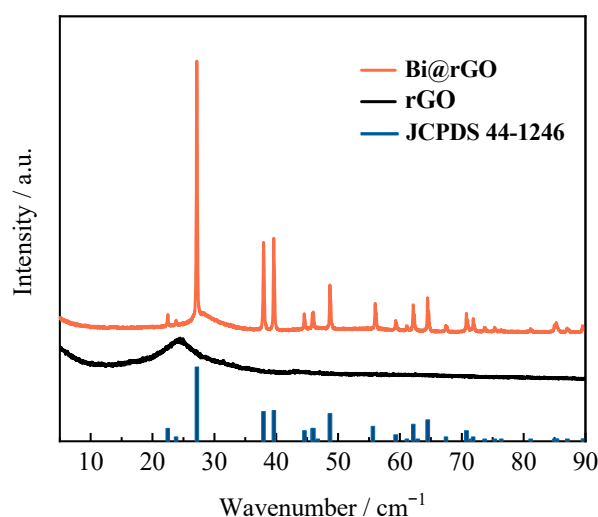


Figure A1. XRD patterns of Bi@rGO, rGO and JCPDS 44-1246 (rhombohedral Bi).

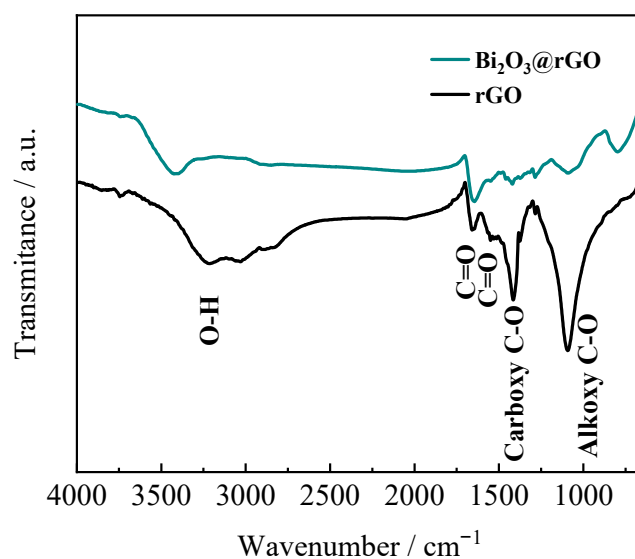


Figure A2. FTIR spectra of Bi₂O₃@rGO and GO.

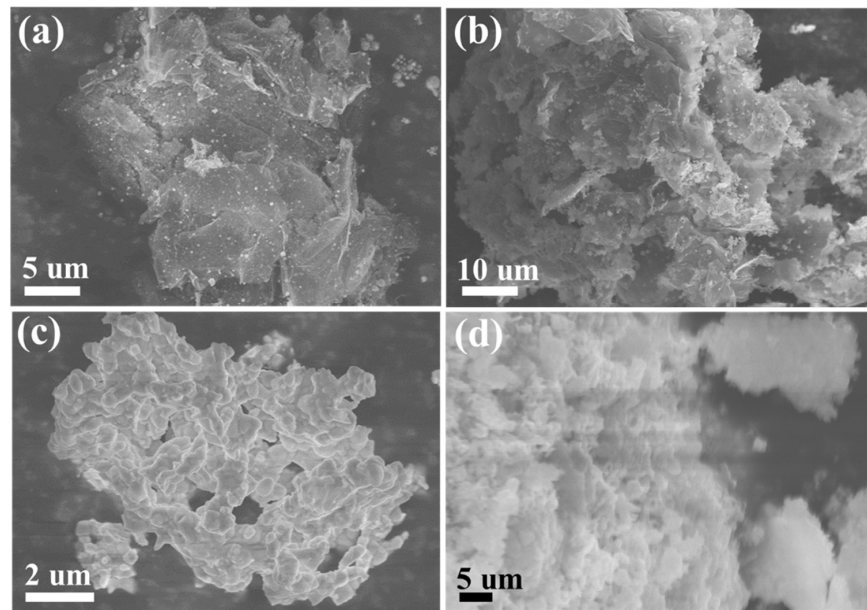


Figure A3. SEM of (a) Bi₂O₃@rGO, (b) Bi@rGO, (c) Bi₂O₃ and (d) Bi.

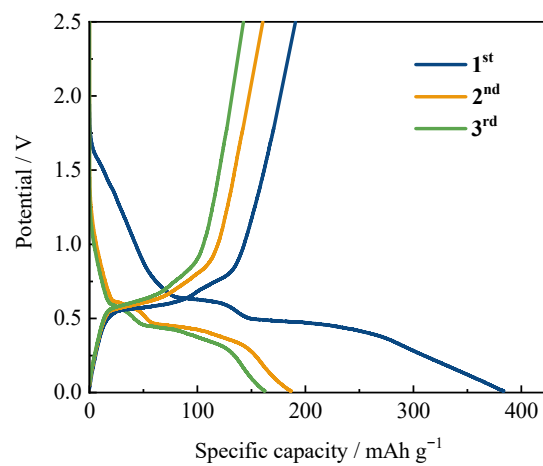


Figure A4. Charge-discharge profiles of Bi₂O₃.

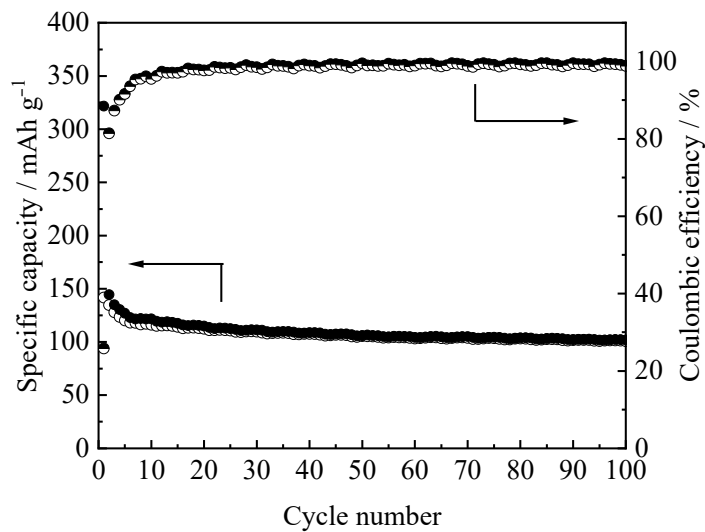


Figure A5. Cycle performance of rGO at 50 mA g⁻¹.

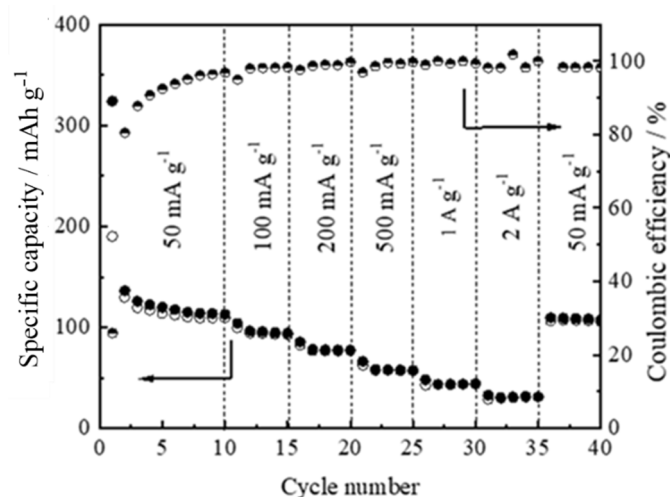


Figure A6. Rate performance of rGO.

References

1. Yang, Y.; Okonkwo, E.G.; Huang, G.; Xu, S.; Sun, W.; He, Y. On the sustainability of lithium ion battery industry—A review and perspective. *Energy Storage Mater.* **2021**, *36*, 186–212. [\[CrossRef\]](#)
2. Wu, J.; Ihsan-Ul-Haq, M.; Ciucci, F.; Huang, B.; Kim, J.-K. Rationally designed nanostructured metal chalcogenides for advanced sodium-ion batteries. *Energy Storage Mater.* **2021**, *34*, 582–628. [\[CrossRef\]](#)
3. Sun, Y.; Shi, P.; Chen, J.; Wu, Q.; Liang, X.; Rui, X.; Xiang, H.; Yu, Y. Development and challenge of advanced nonaqueous sodium ion batteries. *Energy Chem.* **2020**, *2*, 100031. [\[CrossRef\]](#)
4. Zhang, W.; Zhang, F.; Ming, F.; Alshareef, H.N. Sodium-ion battery anodes: Status and future trends. *Energy Chem.* **2019**, *1*, 100012. [\[CrossRef\]](#)
5. Li, Y.; Pu, Z.; Sun, Q.; Pan, N. A review on novel activation strategy on carbonaceous materials with special morphology/texture for electrochemical storage. *J. Energy Chem.* **2021**, *60*, 572–590. [\[CrossRef\]](#)
6. Zhang, W.; Sun, M.; Yin, J.; Wang, W.; Huang, G.; Qiu, X.; Schwingenschlög, U.; Alshareef, H.N. Rational design of carbon anodes by catalytic pyrolysis of graphitic carbon nitride for efficient storage of Na and K mobile ions. *Nano Energy* **2021**, *87*, 106184. [\[CrossRef\]](#)
7. Wang, Y.; Liu, J.; Chen, X.; Kang, B.; Wang, H.-E.; Xiong, P.; Chen, Q.; Wei, M.; Li, N.; Qian, Q.; et al. Structural engineering of tin sulfides anchored on nitrogen/phosphorus dual-doped carbon nanofibres in sodium/potassium-ion batteries. *Carbon* **2022**, *189*, 46–56. [\[CrossRef\]](#)
8. Wang, D.; Cao, L.; Luo, D.; Gao, R.; Li, H.; Wang, D.; Sun, G.; Zhao, Z.; Li, N.; Zhang, Y.; et al. Chain mail heterostructured hydrangea-like binary metal sulfides for high efficiency sodium ion battery. *Nano Energy* **2021**, *87*, 106185. [\[CrossRef\]](#)
9. Fang, S.; Bresser, D.; Passerini, S. Transition Metal Oxide Anodes for Electrochemical Energy Storage in Lithium- and Sodium-Ion Batteries. *Adv. Energy Mater.* **2020**, *10*, 1902485. [\[CrossRef\]](#)
10. Li, Y.; Xu, Y.; Yang, W.; Shen, W.; Xue, H.; Pang, H. MOF-Derived Metal Oxide Composites for Advanced Electrochemical Energy Storage. *Small* **2018**, *14*, 1704435. [\[CrossRef\]](#)
11. Zhang, W.; Liu, T.; Wang, Y.; Liu, Y.; Nai, J.; Zhang, L.; Sheng, O.; Tao, X. Strategies to improve the performance of phosphide anodes in sodium-ion batteries. *Nano Energy* **2021**, *90*, 106475. [\[CrossRef\]](#)
12. Chang, G.; Zhao, Y.; Dong, L.; Wilkinson, D.P.; Zhang, L.; Shao, Q.; Yan, W.; Sun, X.; Zhang, J. A review of phosphorus and phosphides as anode materials for advanced sodium-ion batteries. *J. Mater. Chem. A* **2020**, *8*, 4996–5048. [\[CrossRef\]](#)
13. Zhang, J.; Lin, X.; Xue, D.; Xu, B.; Long, D.; Xue, F.; Duan, X.; Ye, W.; Wang, M.; Li, Q. A generalized strategy for the synthesis of two-dimensional metal oxide nanosheets based on a thermoregulated phase transition. *Nanoscale* **2019**, *11*, 3200–3207. [\[CrossRef\]](#) [\[PubMed\]](#)
14. Fang, W.; Fan, L.; Zhang, Y.; Zhang, Q.; Yin, Y.; Zhang, N.; Sun, K. Synthesis of carbon coated Bi₂O₃ nanocomposite anode for sodium-ion batteries. *Ceram. Int.* **2017**, *43*, 8819–8823. [\[CrossRef\]](#)
15. Deng, Z.; Liu, T.; Chen, T.; Jiang, J.; Yang, W.; Guo, J.; Zhao, J.; Wang, H.; Gao, L. Enhanced Electrochemical Performances of Bi₂O₃/rGO Nanocomposite via Chemical Bonding as Anode Materials for Lithium-Ion Batteries. *Appl. Mater. Interfaces* **2017**, *9*, 12469–12477. [\[CrossRef\]](#)
16. Kim, M.-K.; Yu, S.-H.; Jin, A.; Kim, J.; Ko, I.-H.; Lee, K.-S.; Mun, J.; Sung, Y.-E. Bismuth oxide as a high capacity anode material for sodium-ion batteries. *Chem. Commun.* **2016**, *52*, 11775–11778. [\[CrossRef\]](#)
17. Din, M.A.U.; Li, C.; Zhang, L.; Han, C.; Li, B. Recent progress and challenges on the bismuth-based anode for sodium-ion batteries and potassium-ion batteries. *Mater. Today Phys.* **2021**, *21*, 100486. [\[CrossRef\]](#)

18. Wang, W.; Xiao, Y.; Li, X.; Cheng, Q.; Wang, G. Bismuth oxide self-standing anodes with concomitant carbon dots welded graphene layer for enhanced performance supercapacitor-battery hybrid devices. *Chem. Eng. J.* **2019**, *371*, 327–336. [[CrossRef](#)]
19. Qi, Q.; Zhang, H.; Zhang, P.; Bao, Z.; Zheng, W.; Tian, W.; Zhang, W.; Zhou, M.; Sun, M.Z. Self-assembled sandwich hollow porous carbon sphere @ MXene composites as superior LiS battery cathode hosts. *2D Mater.* **2020**, *7*, 025049. [[CrossRef](#)]
20. Wang, Z.; Duana, C.; Wang, D.; Donga, K.; Luoabc, S.; Liuabc, Y.; Wang, Q.; Zhangabc, Y.; Haoabc, A. BiSb@Bi₂O₃/SbO_x encapsulated in porous carbon as anode materials for sodium/potassium-ion batteries with a high pseudocapacitive contribution. *J. Colloid Interface Sci.* **2020**, *580*, 429–438. [[CrossRef](#)]
21. Yin, H.; Cao, M.-L.; Yu, X.-X.; Zhao, H.; Shen, Y.; Li, C.; Zhu, M.-Q. Self-standing Bi₂O₃ nanoparticles/carbon nanofiber hybrid films as a binder-free anode for flexible sodium-ion batteries. *Mater. Chem. Front.* **2017**, *1*, 1615–1621. [[CrossRef](#)]
22. Liu, K.M.; Wu, C.B.; Joung, S.J.; Tsai, W.P.; Su, K.Y. Metal-organic framework composites for energy conversion and storage. *J. Semicond.* **2020**, *41*, 091707. [[CrossRef](#)]
23. Zhang, H.; Huang, Y.; Ming, H.; Cao, G.; Zhang, W.; Ming, J.; Chen, R. Recent advances in nanostructured carbon for sodium-ion batteries. *J. Mater. Chem. A* **2020**, *8*, 1604–1630. [[CrossRef](#)]
24. Wang, L.; Wei, Z.; Mao, M.; Wang, H.; Li, Y.; Ma, J. Metal oxide/graphene composite anode materials for sodium-ion batteries. *Energy Storage Mater.* **2019**, *16*, 434–454. [[CrossRef](#)]
25. Kong, Z.; Liu, X.; Wang, T.; Fu, A.; Li, Y.; Guo, P.; Guo, Y.-G.; Li, H.; Zhao, X.S. Three-dimensional hollow spheres of porous SnO₂/rGO composite as high-performance anode for sodium ion batteries. *Appl. Surf. Sci.* **2019**, *479*, 198–208. [[CrossRef](#)]
26. Zheng, C.; Xu, X.; Lin, Q.; Chen, Y.; Guo, Z.; Jian, B.; Li, N.; Zhang, H.; Lv, W. Confined growth of Fe₂O₃ nanoparticles by holey graphene for enhanced sodium-ion storage. *Carbon* **2021**, *176*, 31–38. [[CrossRef](#)]
27. Hummers, W.S., Jr.; Offeman, R.E. Preparation of Graphitic Oxide. *Chem. Soc.* **1985**, *80*, 1339. [[CrossRef](#)]
28. Cote, L.J.; Kim, F.; Huang, J. Langmuir-Blodgett Assembly of Graphite Oxide Single Layers. *J. Am. Chem. Soc.* **2009**, *131*, 1043–1049. [[CrossRef](#)]
29. Qin, T.; Zhang, X.; Wang, D.; Deng, T.; Wang, H.; Liu, X.; Shi, X.; Li, Z.; Chen, H.; Meng, X.; et al. Oxygen Vacancies Boost δ-Bi₂O₃ as High-Performance Electrode for Rechargeable Aqueous Batteries. *Appl. Mater. Interfaces* **2018**, *11*, 2103–2111. [[CrossRef](#)]
30. Zhao, Z.; Ye, Y.; Zhu, W.; Xiao, L.; Deng, B.; Liu, J. Bismuth oxide nanoflake@carbon film: A free-standing battery-type electrode for aqueous sodium ion hybrid supercapacitors. *Chin. Chem. Lett.* **2018**, *29*, 629–632. [[CrossRef](#)]
31. Nithya, C. Bi₂O₃@Reduced Graphene Oxide Nanocomposite: An Anode Material for Sodium-Ion Storage. *ChemPlusChem* **2015**, *80*, 1000–1006. [[CrossRef](#)]
32. Hwang, J.; Park, J.-H.; Chung, K.Y.; Kim, J. One-pot synthesis of Bi-reduced graphene oxide composite using supercritical acetone as anode for Na-ion batteries. *Chem. Eng. J.* **2020**, *387*, 124111. [[CrossRef](#)]
33. Xiong, P.; Bai, P.; Li, A.; Li, B.; Cheng, M.; Chen, Y.; Huang, S.; Jiang, Q.; Bu, X.; Xu, Y. Bismuth Nanoparticle@Carbon Composite Anodes for Ultralong Cycle Life and High-Rate Sodium-Ion Batteries. *Adv. Mater.* **2019**, *31*, 1904771. [[CrossRef](#)] [[PubMed](#)]
34. Li, D.; Yan, D.; Zhang, X.; Li, J.; Lu, T.; Pan, L. Porous CuO/reduced graphene oxide composites synthesized from metal-organic frameworks as anodes for high-performance sodium-ion batteries. *J. Colloid Interface Sci.* **2017**, *497*, 350–358. [[CrossRef](#)] [[PubMed](#)]